OPEN ACCESS
IOP Publishing
Superconductor Science and Technology
Supercond. Sci. Technol. **33** (2020) 035007 (15pp)
https://doi.org/10.1088/1361-6668/ab6bfe

The transient voltage response of ReBCO coated conductors exhibiting dynamic resistance

J M Brooks[1,3], M D Ainslie[2], Zhenan Jiang[1], A E Pantoja[1], R A Badcock[1] and C W Bumby[1,3]

[1] Robinson Research Institute, Faculty of Engineering, Victoria University of Wellington, New Zealand
[2] Bulk Superconductivity Group, Department of Engineering, University of Cambridge, United Kingdom

E-mail: gus.brooks@vuw.ac.nz and chris.bumby@vuw.ac.nz

Received 5 November 2019, revised 4 December 2019
Accepted for publication 15 January 2020
Published 4 February 2020

Abstract

Dynamic resistance can be observed in a superconducting tape carrying a DC current which is exposed to an oscillating magnetic field. This effect is attributed to the interaction between the transport current and moving fluxons, and can occur in various superconducting components including high temperature superconducting (HTS) flux pumps, fast-ramping magnets and HTS rotating machines. Although conventionally expressed in terms of a DC 'resistance,' the phenomenon is inherently transient in nature, and the voltage drop across the superconductor follows a time-dependent periodic waveform. Here we present experimental measurements of the dynamic resistance of different REBCO tapes carrying a DC current and exposed to an oscillating perpendicular field. Measurements of both the transient voltage waveforms and the time-averaged DC resistances are compared with numerical finite element simulations obtained using the *H*-formulation. We observe clear variations between the voltage response from different tapes, which can be understood in terms of their differing $J_c(B, \theta)$ dependence. In particular, a key feature of the experimentally measured waveforms is the emergence of a split 'double peak' at higher applied fields. Graphical visualisations of the finite element data show that this coincides with a periodic increase in $J_c(B, \theta)$ throughout the tape. This occurs during each cycle at those times when the applied field falls below the shielding threshold of the tape (as the penetrating field within the tape then approaches zero). Our findings show that models which assume a *constant* J_c irrespective of local field strength cannot capture the full range of behaviour observed by experiment. This emphasises the importance of employing experimentally measured $J_c(B, \theta)$ data when simulating transient effects in HTS materials.

Keywords: dynamic resistance, AC loss, coated conductor, *H*-formulation

(Some figures may appear in colour only in the online journal)

1. Introduction

The commercial availability of kilometre-plus lengths of coated conductor REBCO tapes enables the production of large-scale high temperature superconducting (HTS) magnets and power systems. Such devices include DC and AC magnets, transformers and rotating machines. When superconducting devices are exposed to time-varying fields and currents, dissipative interactions occur between moving

[3] Authors to whom any correspondence should be addressed.

Original content from this work may be used under the terms of the Creative Commons Attribution 3.0 licence. Any further distribution of this work must maintain attribution to the author(s) and the title of the work, journal citation and DOI.

 © 2020 The Author(s). Published by IOP Publishing Ltd Printed in the UK

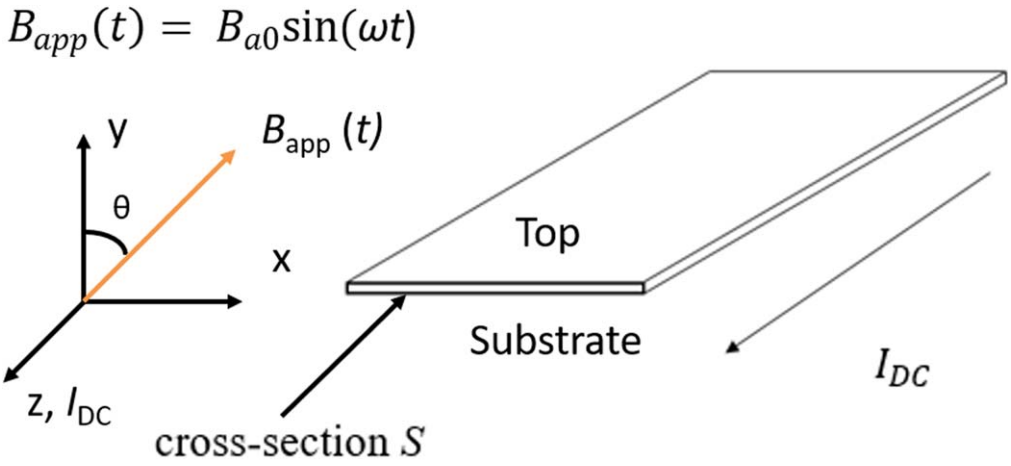

Figure 1. Schematic showing the orientation of axes, magnetic field and transport current within the REBCO tape.

fluxons and the transport current. Here we investigate the AC loss that occurs when a superconductor carries a DC transport current whilst simultaneously exposed to an AC magnetic field. Under these conditions, a DC electrical resistance is observed, termed the dynamic resistance. This DC resistance is conventionally discussed in terms of the net volume of flux which traverses the DC current carrying region of the superconductor during each cycle [1–4]. Understanding the origin and behaviour of dynamic loss is relevant to optimising the management of heat dissipation for various HTS applications. In addition, dynamic resistance has also been identified to play a key role in the operating mechanism of HTS flux pumps [5–9].

Dynamic resistance is generally considered a DC effect [10–15], although experimental measurements of the time dependence of the measured voltage have been reported in [16, 17]. Exact analytical solutions for the magnetic field and current density in a superconducting strip carrying a DC transport current exposed to an oscillating magnetic have previously been derived from the critical state model (in which J_c is assumed to be constant) [18–21]. These were used in [22] to suggest the following picture. When a superconducting thin film is exposed to an alternating magnetic field, magnetisation currents flow in the outer regions of the conductor. If the amplitude of the applied field is less than some sample-dependent threshold value B_{th}, the applied field fails to fully penetrate the conductor and there is an interior region of frozen flux. Any transport current flowing in this region does not experience a change in magnetic field and is able to flow with zero electrical resistance. However, once B_{th} is exceeded, this interior region experiences a change in flux and a non-zero dynamic resistance is observed, which is due to the work done by the power supply in applying a Lorentz force to the net flux traversing the film. Both [14, 22] state that, for a superconducting strip of width $2w$ and thickness d filling the space $|x| \leqslant w$, $|y| \leqslant d/2$ and $|z| < \infty$, centred at $(x, y) = (0, 0)$ and experiencing a homogenous magnetic field $B_{app}(t) = B_{a0}\ \sin(\omega t)$ applied along the y axis, the total dynamic resistance per cycle is given by

$$\frac{R_{dyn}}{fL} = \frac{4w}{I_{c0}}(B_{a0} - B_{th})\,. \tag{1}$$

Two alternative analytical models have been suggested, which give different dependencies of B_{th} on the reduced current $i = I_{DC}/I_{c0}$

$$B_{th} = \frac{4.9284\mu_0 J_{c0} d}{2\pi}(1 - i)\,, \tag{2}$$

$$B_{th} = \frac{\mu_0 J_{c0} d}{2\pi}\left[\frac{1}{i}\ln\left(\frac{1+i}{1-i}\right) + \ln\left(\frac{1-i^2}{4i^2}\right)\right]. \tag{3}$$

Equations (2) and (3) come from [14, 22] respectively. The values obtained for B_{th} from each equation are found to closely agree for $i \gtrsim 0.1$, but diverge at smaller transport currents [22].

Here we present a detailed study of both the time-dependent (instantaneous) and time-averaged (DC) dynamic resistance which occurs in a REBCO coated conductor tape. Experimental measurements are used to validate a computational model based on the *H*-formulation. This model is then used to probe the time evolution of current and field within the tape, and to illustrate effect of the $J_c(B, \theta)$ dependence of the tape on the transient dynamic loss. We present visualisations of the local current, B-field and E-field within the superconducting tape, which reveal the complex behaviour over each cycle. Importantly, this improved and detailed understanding now allows key features in the transient induced voltage response to be understood, and provides key insights into the role of $J_c(B, \theta)$ and $n(B, \theta)$ on the absolute magnitude of the observed DC resistance.

2. The *H*-formulation finite element method

We have computed the dynamic resistance which arises in a REBCO tape using the finite element architecture shown in figure 1. Time-dependent numerical calculations are performed in COMSOL Multiphysics 5.3a® using a 2D *H*-formulation model in the *xy*-plane (this assumes an infinitely long superconducting tape in the *z* direction). The solutions are obtained

by solving Faraday's law (4) and Ampere's law (5)

$$\nabla \times \boldsymbol{E} = -\mu_0 \frac{\partial(\mu_r \boldsymbol{H})}{\partial t}, \tag{4}$$

$$\nabla \times \boldsymbol{H} = \boldsymbol{J}, \tag{5}$$

where $\boldsymbol{H} = [H_x, H_y]$ represents the magnetic field strength, $\boldsymbol{J} = [J_z]$ the current density and $\boldsymbol{E} = [E_z]$ the electric field. The permeability of free space is given by μ_0 and the relative permeability of the superconducting domain is assumed as $\mu_r = 1$.

The electrical properties of the superconductor are modelled by an $\boldsymbol{E}$–$\boldsymbol{J}$ power law [23, 24]

$$\boldsymbol{E} = \frac{E_0}{J_c(B, \theta)} \left| \frac{J}{J_c(B, \theta)} \right|^{n(B,\theta)-1} \boldsymbol{J}, \tag{6}$$

where E_0 is the characteristic electric field, 1 μV cm^{-1}, and θ is the orientation of the magnetic field relative to the sample, as shown in figure 1. Two different sets of experimental data describing $J_c(B, \theta)$ and $n(B, \theta)$, taken from two different tapes, are investigated in this work, as described in section 4.1.

Meshing of the FE model consists of 200 elements along the width of the superconducting domain (in the x-direction), and 3 elements across its thickness (in the y-direction). This ensures that the computational time required for the models remains practical, while retaining enough resolution at the surface of the superconductor when simulating the current distribution. In the surrounding sub-domain, a free triangular mesh is used. The subdomain boundary is sufficiently far away such that the normal component of the magnetic field due to the superconductor is zero. In the non-superconducting subdomain, we solve a linear Ohm's law with the resistivity set to 1 Ωm. The computational model assumes that all losses occur entirely in the HTS layer, a reasonable assumption for low AC frequencies (e.g. $\lesssim$ 1 kHz) where the eddy-current losses in the metallic layers are negligible [25, 26]. The HTS layer is also assumed to remain at a constant temperature. Thus, only contributions from the superconducting layer are included when calculating the dynamic resistance, and no temperature dependence is included.

The current and field distributions within the tape are computed using a two stage process. First, a DC transport current is applied to the superconductor, ramped from zero to the required value. Following this, a sinusoidal perpendicular magnetic field is then applied to the sample for two and a half AC field oscillations. Subsequent data analysis neglects the initial half cycle during which the superconducting strip is magnetised from its virgin state. This ensures that the computed values are periodic with the applied magnetic field.

A DC transport current, I_T, is applied via an integral constraint applied to the superconducting cross-section S of the form

$$I_T = \int_S \boldsymbol{J} \cdot \mathrm{d}\mathbf{S} = I_{\mathrm{app}}(t). \tag{7}$$

In the first stage of the computation, $I_{\mathrm{app}}(t)$ is a linear ramp function with a gradient of 10 A s^{-1}. This ramp function is run until the DC transport current is equal to the self-field critical current I_{c0}. Once completed, we have access to the solution at all stored time intervals and reduced currents. The second stage is then initiated using the solution which corresponds to the specified reduced current under study (i.e. $i = I_T/I_c = 0.3$, 0.5 and 0.7). The sinusoidal perpendicular AC magnetic field of the form $B_{\mathrm{app}} = B_{a0}\sin(\omega t)$ is applied using COMSOL's magnetic field boundary condition.

The dynamic resistance, R_{dyn}, results in the development of a voltage drop, ΔV, along the z-direction of the coated conductor. This is calculated from the 2D FE model using:

$$\Delta V(t) = L \cdot \frac{\partial V(t)}{\partial z}, \tag{8}$$

where L is the length of the conductor in the z-direction.

Dynamic resistance is a low-frequency quasi-static phenomenon, such that the voltage drop is simply the difference in electrostatic potential across the conductor. In the Coulomb gauge (defined by $\nabla \cdot \boldsymbol{A} = 0$, such that $\nabla^2 \boldsymbol{A} = \mu_0 J$), the electrostatic potential is equivalent to the electric scalar potential, such that [25, 26]

$$\nabla V(t) = \boldsymbol{E}(t) + \frac{\partial \boldsymbol{A}(t)}{\partial t}. \tag{9}$$

(Note that taking the divergence of both sides of equation (9) yields the familiar definition of the electrostatic potential, $\nabla^2 V = \nabla \cdot \boldsymbol{E} = \rho/\varepsilon$.)

We obtain the magnetic vector potential, $\boldsymbol{A}$, from the inverse curl of $\mathbf{B}$, and by specifying a Dirichlet boundary condition that A_z is equal to $-B_y x$ along the boundary of the surrounding air subdomain. The 2D FE geometry constrains currents from flowing in the plane of the model, such that $J_x = J_y = E_x = E_y = {}_{Ax} = A_y = 0$. As a result, equation (9) simplifies solely to the z components, with $\partial V/\partial z$ constant throughout the model plane for each moment in time. However, it should be noted that both $E_z(x, y, t)$ and $A_z(x, y, t)$ are functions of x and y, and hence do vary across the plane (see, for example, figure 6(c)).

To minimise numerical error, we use the spatially-averaged value of $\Delta V(t)$ across the HTS cross-section, calculated using equation (10):

$$\Delta V(t) = L\frac{\partial V(t)}{\partial z} = \frac{-1}{S}\int_S (E_z + \partial\, {}_t A_z) \cdot \mathrm{d}S. \tag{10}$$

The time-averaged DC dynamic resistance, in units of $\mu\Omega$/m/cycle, is then calculated by integrating ΔV over a single cycle of the applied field and dividing by the transport current

$$R_{\mathrm{dyn}} = \frac{1}{I_T}\int_0^{1/f} \Delta V dt. \tag{11}$$

It is noteworthy that all dissipation within the superconductor is fully described by the E–J relation given in equation (6). As a result, the A-vector contribution can in fact be omitted from equations (10) and (11) without loss of accuracy [27].

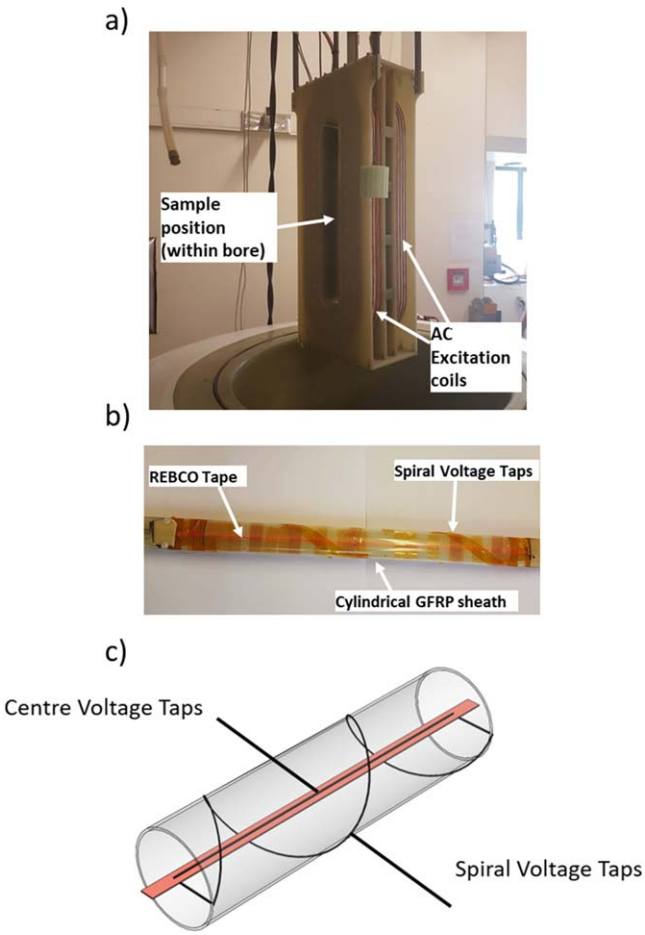

Figure 2. (a) Photograph of the experimental apparatus used to perform dynamic resistance measurements. (b) Photograph of the experimental sample holder in which a REBCO tape is mounted (within the cylindrical sheath). (c) Schematic diagram showing the geometry of the sample voltage taps used in the experimental sample holder. Both consist of a twisted pair of copper wires. The centre voltage taps run along all the broad face of the conductor while the spiral pair are wound around a cylindrical sheath surrounding the sample.

3. Experimental methods

3.1. Dynamic resistance measurements

The dynamic resistance measurements were performed using 30 cm lengths of coated conductor tape mounted on a G10 sample board. This was positioned between a pair of copper-wound racetrack coils capable of producing AC magnetic fields with a peak amplitude up to 100 mT. Two separate voltage measurements were obtained using two pairs of voltage taps 20 cm apart. One pair was helically wound around a cylindrical sheath encapsulating the sample board, whilst the other was a twisted pair running up the centre of the sample. The arrangement of these two voltage taps are shown in figure 2. The measurement procedure was as follows. Firstly, the magnet was energised, and a zero-transport current voltage measurement was taken over two seconds. The transport current through the sample was then increased to the reduced current values $i = 0.3$, 0.5, and 0.7, and voltage measurements were taken for each current. The current was then reset to zero and the magnet re-energised to produce a larger field. This process was repeated until the desired parameter space had been covered. The voltage waveform measured at zero transport current for each B_{a0} is due solely to inductive pick-up from the loop formed by the connecting leads between the sample and instruments. This provided a calibration baseline which was then subtracted from subsequent measurements performed at each non-zero current, in order to yield a signal solely due to the interaction of the AC field with the transport current flowing through the coated conductor tape. The measured voltage signal passed through an NF Electronics 5325 Isolation Amplifier before being measured by an NI DAQ USB-6210 module, recording at a sampling rate of 50 kHz. The collected waveforms were then digitally processed to produce an averaged single cycle waveform for comparison to the model results. The DC resistance was obtained through time-averaging the voltage waveform over this full cycle.

3.2. Coated conductor samples

Two different samples of REBCO tape were investigated in this study: SuperPower SCS4050-AP and SuNAM HCN04200 with specifications given in [30, 31]. Measurements of the $J_c(B, \theta)$ and $n(B, \theta)$ parameters for each tape were made using the Super Current instrument at the Robinson Research Institute [28, 29]. Experimental measurements were made at 77 K on short length samples (~5–7 cm), in applied magnetic fields up to 500 mT and obtained for a full 360° range of field orientations at 5° increments. The measured values are shown in figure 3, which illustrates the contrastingly different dependencies of critical current upon applied magnetic field for each tape. Both tapes were four mm wide with the superconducting layer being either 1.3 μm or 1 μm thick, for the SuNAM and SuperPower tapes, respectively. The SuNAM tape had a self-field I_{c0} of 205.5 A and its $J_c(B, \theta)$ behaviour is symmetric about $\theta = 180°$, and periodic such that $I_c(B, \theta) \approx I_c(B, \theta + 180°)$. In contrast, the SuperPower tape had an I_{c0} value of 105.6 A and the measured critical current did not exhibit a symmetry plane with respect to the angle of the applied field.

4. Model and experimental results

4.1. DC values for the dynamic resistance

Figure 4 shows the experimentally measured DC dynamic resistance, R_{dyn}, per cycle obtained at a frequency of 118.66 Hz for three different values of i for both tapes, and using the two different sets of experimental voltage taps ('spiral' and 'centre'). The R_{dyn} values are plotted as a function of the applied field amplitude B_{a0}. Also plotted are the analytical solutions obtained from equation (1) using either equations (2) or (3) to define the threshold field. Consistent with results reported in [13–15], we see that there is

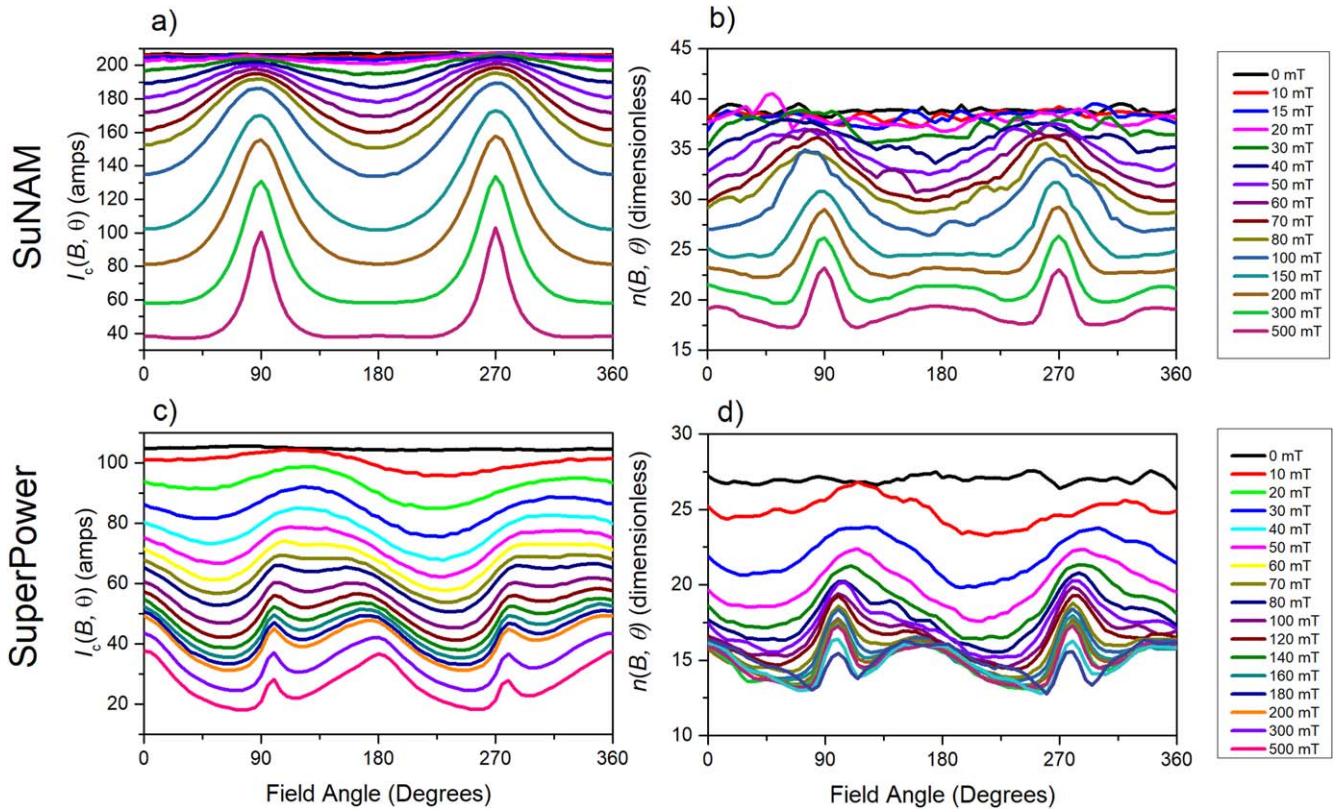

Figure 3. Experimentally measured $I_c(B, \theta)$ and $n(B, \theta)$ data at 77 K as a function of applied magnetic field amplitude and orientation relative to the sample as indicated in figure 1. Plots (a), (b) show the SuNAM data and plots (c), (d) show the Super Power data.

very close agreement between these equations and experimental results.

For comparison, figure 4 also shows the calculated values of R_{dyn} obtained from the numerical model. Simulations have been performed using two different functions for $J_c(B, \theta)$ and $n(B, \theta)$.

(i) *Constant J_c model ($J_c = J_{c0}$)*: in this model, the critical current and n-value are both assumed to be constant at all times, and are set equal to the values measured in zero applied field, i.e. $J_c(B, \theta) = J_{c0}$, $n = 20$. In sections 4.1 and 4.2, a modified version of the *constant J_c* model has also been considered, which uses an artificially high n-value of $n = 200$, as a close approximation to the critical state model.

(ii) *Interpolated $J_c(B, \theta)$ model:* this model uses the experimentally-measured values shown in figure 3. Self-field effects are removed from the experimental measurements by the method described in [30], to provide a set of self-fieldcorrected $J_c(B, \theta)$ values. These describe the local critical current density at each point within the tape, as a function of the total local magnetic field, $\boldsymbol{B}$. Both the J_c and n-values are then input into the numerical model using a two variable interpolation function, as described in [31, 32].

The *interpolated $J_c(B, \theta)$* model is observed to deliver good agreement with experiment, although it does appear to slightly underestimate B_{th} in every case. However, the *constant J_c*, $n = 20$ model diverges substantially from experiment, and significantly understates the magnitude of dR_{dyn}/dB_{a0} at fields above B_{th}. This highlights the importance of including the full $J_c(B, \theta)$ dependence within the FE model. It also raises the question as to why the analytical equations (1)–(3) are so successful, despite employing a constant critical current value. On this point, it is instructive to note that the analytical approaches assume $n \to \infty$, whilst the *constant J_c* FE model uses the realistic finite value of $n = 20$. By contrast, if the FE model is instead run using a much higher n-value of $n = 200$, we obtain results which closely agree with equations (2) and (3). This suggests that the artificially high n-value within the critical state model can compensate for the error introduced by assuming a *constant* J_c. This appears to be a 'happy accident' that holds for the samples and experimental conditions considered here, but it is not clear how applicable these equations would be in other differing situations [12, 16, 33].

4.2. Transient voltage response to a perpendicular sinusoidal field

In addition to DC experimental measurements, transient time-resolved measurements were also performed to obtain the resistive voltage waveform across each sample tape. Figure 5 shows these experimentally-measured voltage waveforms, and compares these with the corresponding waveforms obtained from the numerical simulations using each of the $J_c(B, \theta)$ models. Each plot shows the response over two cycles of the applied field at 118.66 Hz for $i = 0.5$.

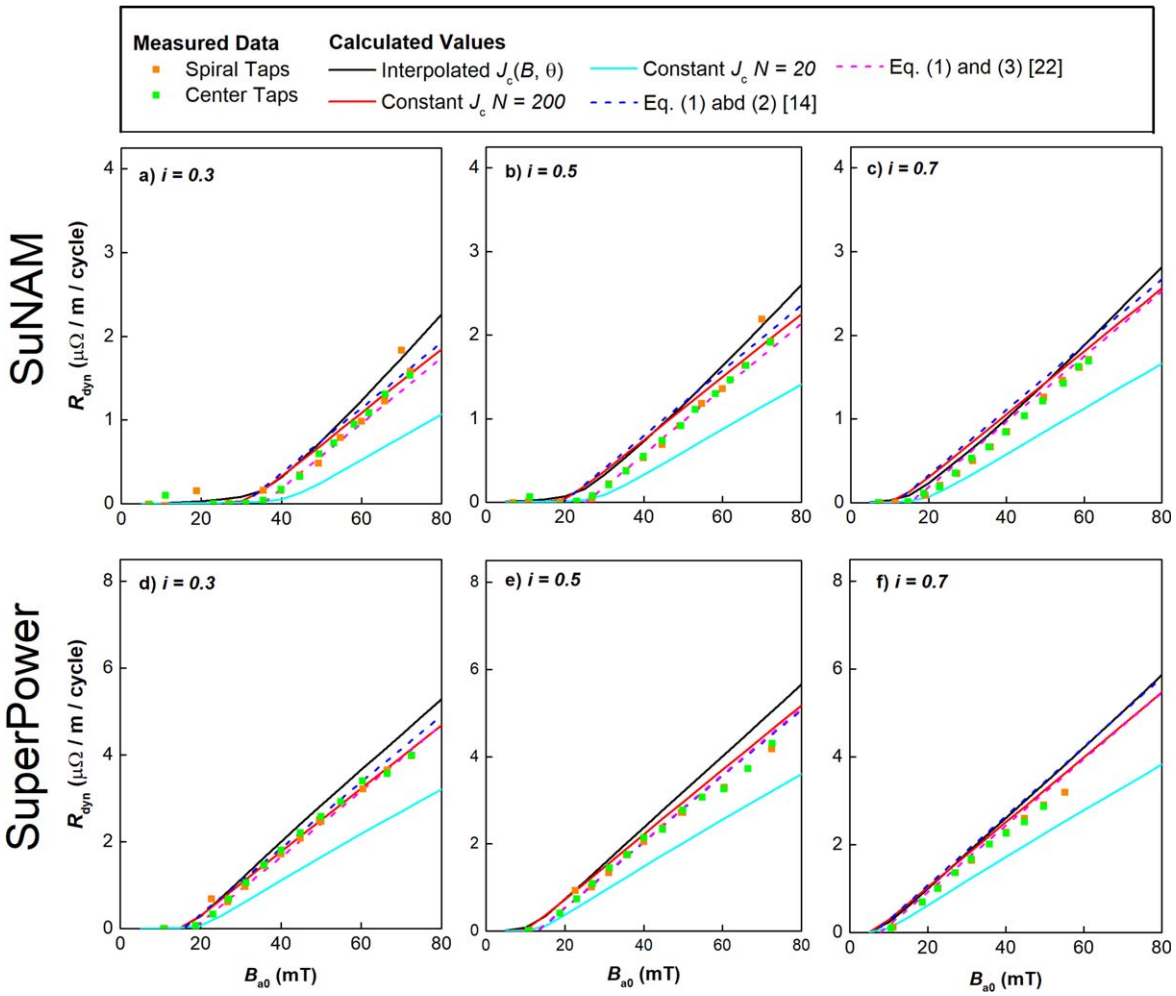

Figure 4. The dynamic resistance per cycle as a function of B_{a0}, for SuNAM (a)–(c) and SuperPower (d)–(f) tapes. The data is given for $i = 0.3$, 0.5 and 0.7 for a frequency, $f = 118.66$ Hz. Experimental data from the spiral and centre voltage taps is shown, alongside values calculated from equations (1)–(3). The numerically-modelled data is also shown for models run using various different functions to describe $J_c(B, \theta)$, namely: *constant* $J_c(n = 20)$, *constant* $J_c(n = 200)$ and *interpolated* $J_c(B, \theta)$.

As expected [3, 17, 27], the numerical models all predict a voltage waveform that is periodic over one half cycle of the applied magnetic field (i.e. its fundamental frequency is twice that of the applied field). This is because applied flux interacts with the transport current whenever the magnitude of the applied field exceeds the shielding capacity of the tape. This occurs during each half cycle, irrespective of the polarity of the applied field. There is a noticeable difference in both the amplitude and shape of the waveforms calculated using *constant* J_c model with $n = 200$ (approximating to the critical state model), versus $n = 20$ (which is close to the actual measured value of n in self-field). In particular, the lower n-value exhibits both a smaller peak amplitude and a smaller peak width. This is the reason that it delivers a lower time-averaged DC resistance (shown in figure 4).

Similar to the *constant* J_c models, the experimental waveform data also shows a doubling of the fundamental frequency of the voltage waveform compared to the applied field. However, several striking differences are also apparent. Most notably, as the magnetic field amplitude increases well above B_{th}, a peak-splitting effect is observed whereby a non-zero minimum appears within each waveform at $B_{app}(t) \sim 0$. The only numerical model which reproduces this feature is the *interpolated* $J_c(B, \theta)$ model [27]. Understanding the origin of this 'peak-splitting' effect requires detailed scrutiny of the current and field distributions, and is explored in the following section.

In addition, the *interpolated* $J_c(B, \theta)$ model for the SuperPower tape also shows a small asymmetry in the amplitude of the voltage peaks observed during the positive and negative half-cycles of applied field. This is due to the asymmetric angular dependence of $J_c(B, \theta)$ for these tapes.

5. Contour plots of sheet currents and fields

The currents and fields present within the REBCO tape vary in both space and time. To graphically visualise the calculated values, it is convenient to consider the equivalent 'sheet value' that would be present in a planar superconductor with infinitesimal thickness in the y-direction. These sheet values are obtained by integrating and averaging over the thickness

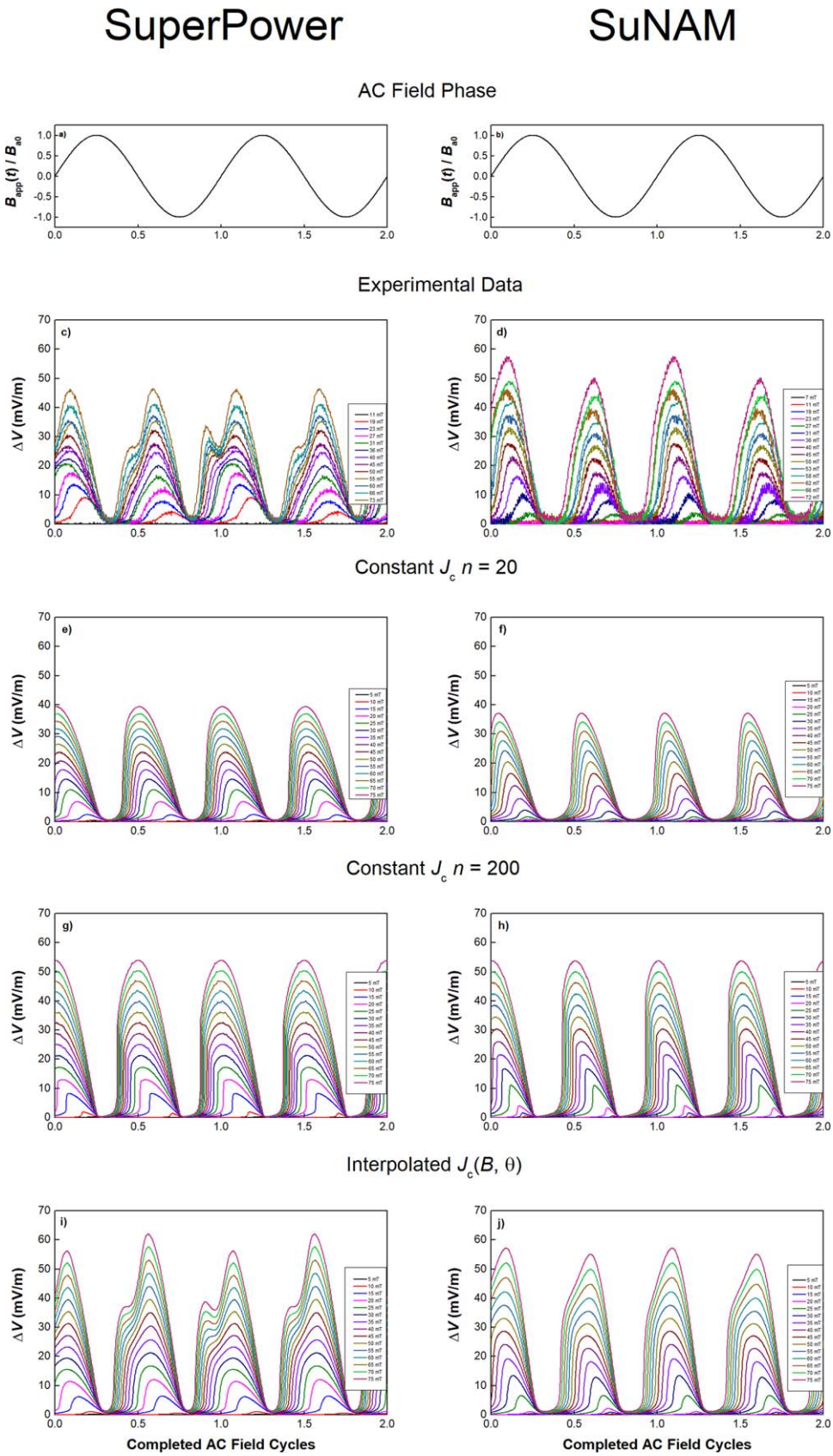

Figure 5. Experimental measurements of the instantaneous voltage, $\Delta V(t)$, across each REBCO tape sample, compared with numerically-modelled values obtained from the *constant* J_c and *interpolated* $J_c(B, \theta)$ models. The SuperPower and SuNAM data are shown in the left and right columns, respectively. All plots are for $i = 0.5$ and $f = 118.66$ Hz. Plots (a) and (b) show the applied field; (c) and (d) show the experimental waveforms; (e) and (f) show the *constant* J_c ($n = 20$) models; (g) and (h) show the *constant* J_c ($n = 200$) models; and (i) and (j) show the *interpolated* $J_c(B, \theta)$ waveforms.

of the superconductor layer, d, as shown in equations (12)–(15). These equations define the sheet current density K_z, the sheet critical current K_c, the sheet perpendicular magnetic field B_y', and the sheet electric field E_z'.

$$B_y'(x, t) = \frac{1}{d}\int_{-\frac{d}{2}}^{\frac{d}{2}} B_y(x, y, t)dy, \tag{12}$$

$$E_z'(x, t) = \frac{1}{d}\int_{-\frac{d}{2}}^{\frac{d}{2}} E_z(x, y, t)dy, \tag{13}$$

$$K_z(x, t) = \int_{-\frac{d}{2}}^{\frac{d}{2}} J_z(x, y, t)dy, \tag{14}$$

$$K_c(x, t) = \int_{-\frac{d}{2}}^{\frac{d}{2}} J_c(x, y, t)dy. \tag{15}$$

The benefit of applying equations (12)–(15) is to transform the 2D arrays calculated for the full cross-section of the tape (i.e. for each position x, y), into 1D arrays which vary in the x-direction only. This then allows the sheet values to be graphically plotted against time in a contour plot. An example is shown in figure 6, where contour plots (a)–(d) show the evolution over two and a half cycles of K_z, B_y', K_c and E_z', calculated using the *constant J_c model*. The x-axis denotes the position across the width of the superconducting tape, which extends from -2 to $+2$ mm. The y-axis value denotes the elapsed time and is plotted in units of ωt such that one full cycle of the applied field has a period of 2π.

The value of the plotted variable at coordinates (x, t) is indicated by the colour-bar scale shown above each plot. In addition, plots (d) and (e) show the variation over time of ΔV and $B_{\mathrm{app}}(t)$. This allows features in these waveforms to be correlated with the spatial distributions shown in each contour plot. In order to illustrate the interpretation of these contour plots, three example moments-in-time are indicated by the horizontal dashed lines labelled $\omega t = 0$, $2\pi/3$, and $4\pi/3$. Figures 6(f)–(n) show line plots of the respective values of K_z, B_y' and E_z', obtained at each of these same moments-in-time, as a function of position across the width of the superconductor. Each line plot is directly equivalent to the contour intersected by the corresponding horizontal dashed line in plots figure 6(a)–(c).

5.1. Constant J_{c0} FE model

Using figure 6, we can now examine the evolution of K_z, B_y', and E_z' in the *constant* J_c model for the SuperPower tape at $i = 0.5$ and $B_{a0} = 100$ mT.

Plot figure 6(a) shows that magnetisation screening currents occur at the edges of the film, but are only distinguishable on the side where the screening currents run anti-parallel to the DC transport current. These screening currents penetrate to an approximately constant depth in each half-cycle. This conforms with the conventional critical state model for dynamic resistance [3, 22], where the transport current is considered to occupy a constant width region at the centre of the tape. Once $\mathrm{d}B_{\mathrm{app}}/\mathrm{d}t$ changes sign (at $\omega t = (2m + 1)\pi/2$ where $m =$ integer), the existing screening current distribution begins to be erased by opposite polarity screening currents which enter from each side. The complete erasure of the previous anti-parallel component of the screening current on one side of the film occurs shortly after $\omega t \approx 2\pi/3$, and coincides with an increase from zero of ΔV in plot (d).

Plot figure 6(b) shows that the behaviour of the magnetic field inside the superconductor broadly follows the periodic behaviour of the applied field, and reaches its maximum and minimum values at approximately the same time as the applied field. These peak internal fields occur at either edge of the superconductor in the region in which screening currents are being erased. At the edge where screening currents run parallel to the transport current, the local magnetic field within the superconductor is much larger than B_{a0}. Once the applied field magnitude passes its peak value (at $\omega t = (2m + 1)\pi/2$), a new screening current distribution is established in the tape. The new screening current distribution then enables a very low magnetic field to persist throughout the superconductor whilst the applied field reverses polarity ($\omega t = m\pi$). At this point flux begins to enter the superconductor again from both edges, whilst a region of zero flux remains spatially-frozen close to the current-reversal zone [14]. This frozen flux gives rise to the characteristic contour spikes (i.e. 'spurs' and 'gullies') which are observed in the B-field plot.

Plot figure 6(c) shows the electric fields generated inside the conductor (in the z-direction). The electric field appears first at the edges, as soon as the screening currents have completed their reversal in each half cycle (e.g. shortly after $\omega t \approx 2\pi/3$). E-fields of opposite polarity occur at each edge, and decrease linearly towards the centre of the conductor (figures 6(h), (k) and (n)). The zone containing E-fields of the same polarity as I_{DC} is always spatially larger than the zone of opposite polarity on the other side of the tape. Both zones achieve their maximum area when the magnitude of $\mathrm{d}B_{\mathrm{app}}/\mathrm{d}t$ is at a maximum, before then decaying again to zero as B_{app} reaches its positive or negative peak.

The linear profile of E_z' across the tape is to be expected for a fully penetrated sample, as $\partial E_z/\partial x = \partial B_y/\partial t$. However, this E-field profile challenges the conventional viewpoint that the current source applies work only to the central region of the tape, where the DC transport current is assumed to flow [3, 14, 22, 34]. Figure 7 shows why this is the case.

Figure 7 illustrates the linear E_z' profile across the tape which occurs at all times in the cycle when flux penetrates throughout the tape. It is clear that the E-field at one edge of the tape is significantly larger than other edge, and hence the net sum of the E-field from both edge regions does not sum to zero. As a result, the net integrated E-field across the tape (shown shaded red) extends all the way to the right-hand edge of the tape. This implies that a DC current source must do work on currents flowing throughout the red shaded region, and not just in the central region from $x = -iw$ to $+iw$ (as described in [3, 9, 22, 34]). This also confirms that it is not possible to spatially distinguish between the transport current and screening currents of the same polarity. In fact, the largest contribution to the dynamic resistance occurs at the

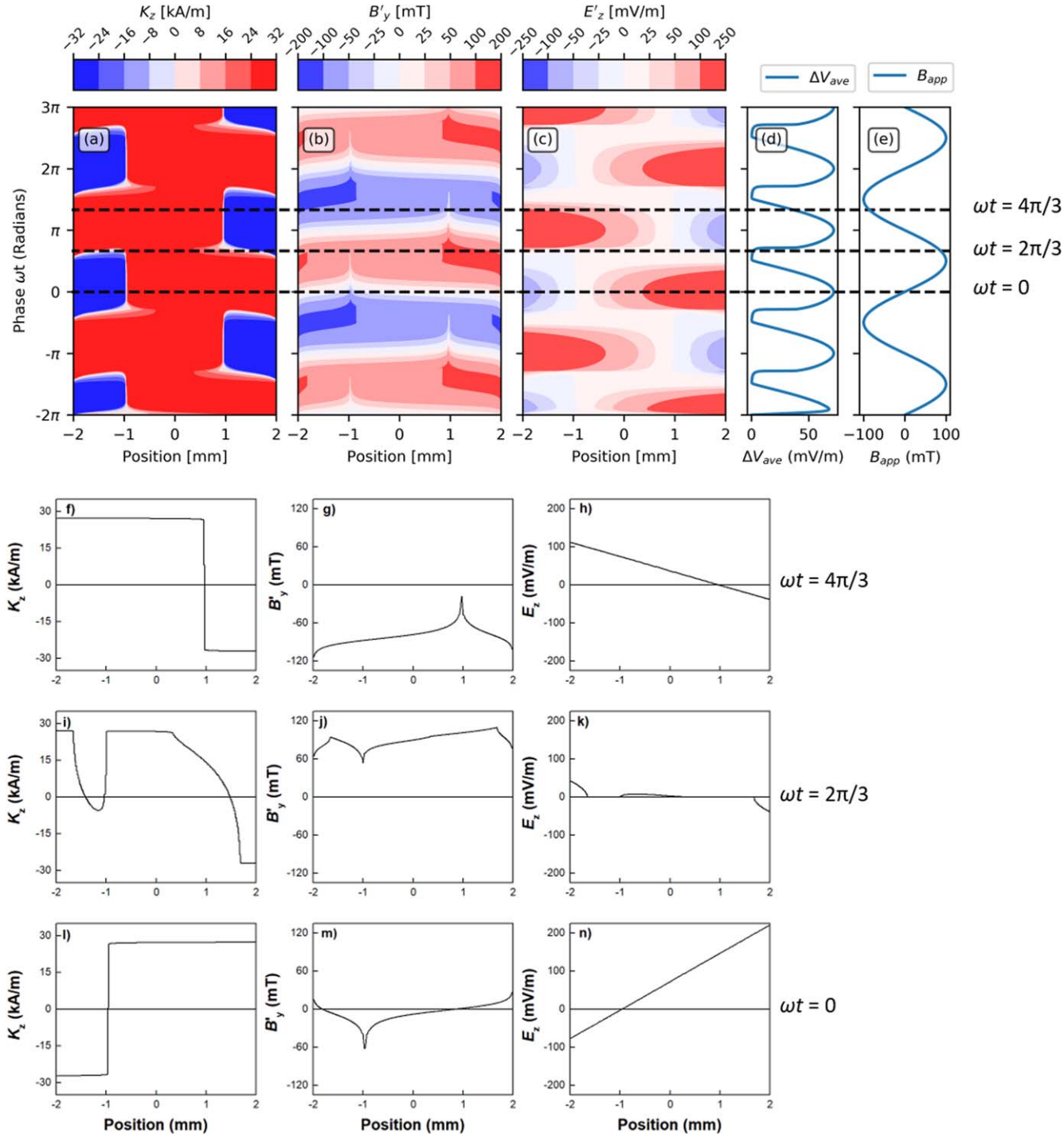

Figure 6. Plots (a)–(c) are contour plots of the time dependence of the sheet variables K_z, B'_y and E'_z across the width of the conductor, calculated for two and a half cycles of the applied field. Data is for the SuperPower *constant* J_c $N = 200$ model with $i = 0.5, f = 118.66$ Hz and $B_{a0} = 100$ mT. These are shown alongside ΔV in plot (d), and the applied field $B_{\mathrm{app}}(t)$ in plot (e). Also shown are the instantaneous profiles across the conductor width for K_z (plots (f)–(l)), B'_y (plots (g)–(m)) and E'_z (plots (h)–(n)) at the three moments-in-time indicated by the dashed lines $\omega t = 0$, $2\pi/3$ and $4\pi/3$.

right-hand edge of the tape in figure 7, contradicting the conventional assumption that solely screening currents flow in this edge region.

This observation raises in turn the interesting question as to why the analytical equations nonetheless yield good estimates of R_{dyn}, despite being based on the flawed assumption of a centrally-localised transport current. The reason for this is that the derivation of equation (1) ultimately requires only that a quantity of net flux traverses a net total transport current, I_{DC} [14]. The differences in equations (2) and (3) relate to different approaches used to estimate the threshold field, but the precise location within the tape at which these

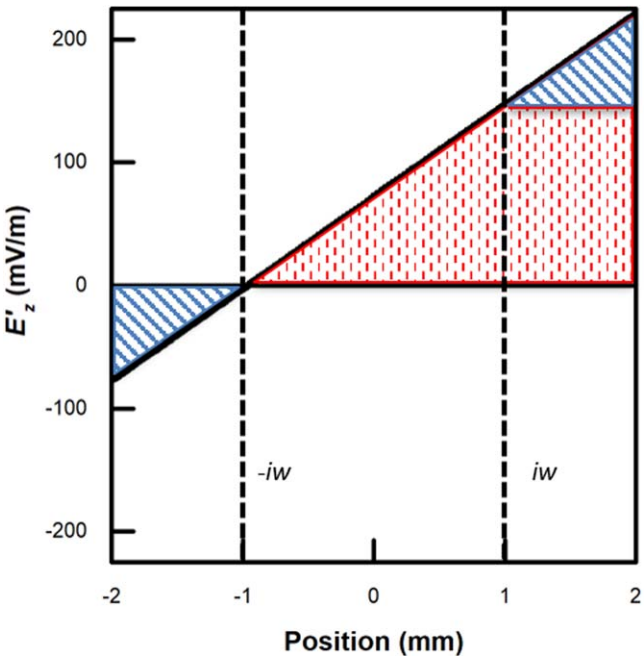

Figure 7. Illustrative plot showing E'_z as a function of position across the conductor width for the *constant* J_c ($n = 200$) model when $i = 0.5$, $B_{a0} = 100$ mT and $\omega t = 2\pi$. The blue-shaded regions represent equal and opposite contributions to the spatially averaged electric field which sum to zero. The red-shaded area shows the net averaged electric field at this moment in the cycle. Note that the same linear behaviour is observed in the $n = 20$ model. The dashed lines show $x = \pm iw$.

interactions occur does not affect the resulting analytical expression.

5.2. Super power interpolated $J_c(B, \theta)$ FEM model

The internal fields and currents calculated by the *interpolated* $J_c(B, \theta)$ model can be visualised in the same fashion as for the *constant* J_c model above. This is shown in figure 8, which also shows the evolution of the sheet critical current K_{cB} in time and space. Unlike the *constant* J_c model, K_c now varies as function of the local field. Modelled data is shown for the same values of reduced current and applied field amplitude as were used above ($i = 0.5$ and $B_{a0} = 100$ mT).

Several different features are apparent in the behaviour of the currents and fields from the *interpolated* $J_c(B, \theta)$ model, compared to the *constant* J_c model for the SuperPower tape. Plot 8(a) shows the evolution of K_z and we see that in this case, screening currents running anti-parallel to the transport current do not occupy a constant width throughout the cycle. Instead, the maximum penetration width of screening currents into the tape occurs when $B_{app} = 0$ ($\omega t = m\pi$), and retreats as B_{app} increases in magnitude. This is because the local K_{cB} decreases as $|B_{app}|$ increases, meaning the transport current must occupy a wider fraction of the tape, and hence reducing the remaining space available for opposing screening currents to flow. As before, the complete erasure of the screening current distribution from the previous half-cycle coincides with ΔV increasing rapidly from zero (e.g. dashed line at $\omega t = 2\pi/3$). We can also see some subtle asymmetries between the current distributions for the positive and negative half-cycles of the applied field, which can be understood in terms of the asymmetric $J_c(B, \theta)$ behaviour of the SuperPower tape shown in plot 2.

Plot figure 8(b) shows the evolution of B'_y within the conductor and its features are very similar to the *constant* J_c model. At the points in the cycle when the screening currents penetrate furthest into the tape ($\omega t = m\pi$), the perpendicular magnetic field is close to zero over the entire width of the conductor. This also corresponds to a peak in the local K_{cB} across the entire cross-section of the conductor—as shown in plot figure 8(c). The low-field contour spikes in B'_y are also present for the *interpolated* $J_c(B, \theta)$ model, but exist for a shorter duration and move outwards to follow the retreating current reversal zone (between $\omega t = m\pi$ and $\omega t = m\pi + \pi/2$).

Plot figure 8(d) shows the E'_z-fields within the conductor, calculated using the *interpolated* $J_c(B, \theta)$ model. These exhibit qualitatively similar behaviour to the *constant* J_c model, but there is a clearly noticeable difference to the shape of the resistive lobes (shown as red in this plot). These now show the 'peak splitting' phenomenon which was previously observed in the ΔV waveforms (see figures 5(c) and (d)). Comparing plots figures 8(c)–(e), we see that the local minima in ΔV at $\omega t = m\pi$, coincides with the double-humped shape of the resistive E'_z-field lobe. We can now deduce that the short-lived reduction in ΔV is caused by the increase in K_c (and equivalently J_c) across the tape at this point in the cycle, which in turn arises because $|B_{app}|$ has become sufficiently small. Equation (9) requires that the increase in local J_c must deliver a decrease in the electric field required for currents to flow at this point in the cycle, and hence the local minima in ΔV.

5.3. SuNAM interpolated $J_c(B, \theta)$ FEM model

Figure 9 shows contour plots of the calculated sheet fields and currents for the SuNAM tape using the *interpolated* $J_c(B, \theta)$ model. The same conditions are used as for the SuperPower tape shown in figure 6 (i.e. $i = 0.5$, $f = 118.66$ Hz and $B_{a0} = 100$ mT).

We see many of the same gross features are apparent as are observed for the SuperPower tape, but there are also some significant differences which arise from the differing $J_c(B, \theta)$ dependences of these two tapes. In particular, the screening currents shown in plot figure 9(a)) do not show a maximum penetration width at $\omega t = m\pi$. There is also no obvious asymmetry in the distribution of currents between positive and negative halves of the oscillating magnetic field.

In figure 9(b) we see that the low field regions near the current reversal zone persist longer than is the case for the SuperPower tape, due to the increased shielding from the larger critical current of the SuNAM tape. This results in a broadening of the periodic increase in K_c visible in plot figure 9(c) that occurs when B_{app} is close to zero ($\omega t = m\pi$). This broadening 'smears out' the effect of the increased K_c, which results in a less pronounced peak splitting of E'_z and ΔV. It should be noted that this smearing effect occurs even

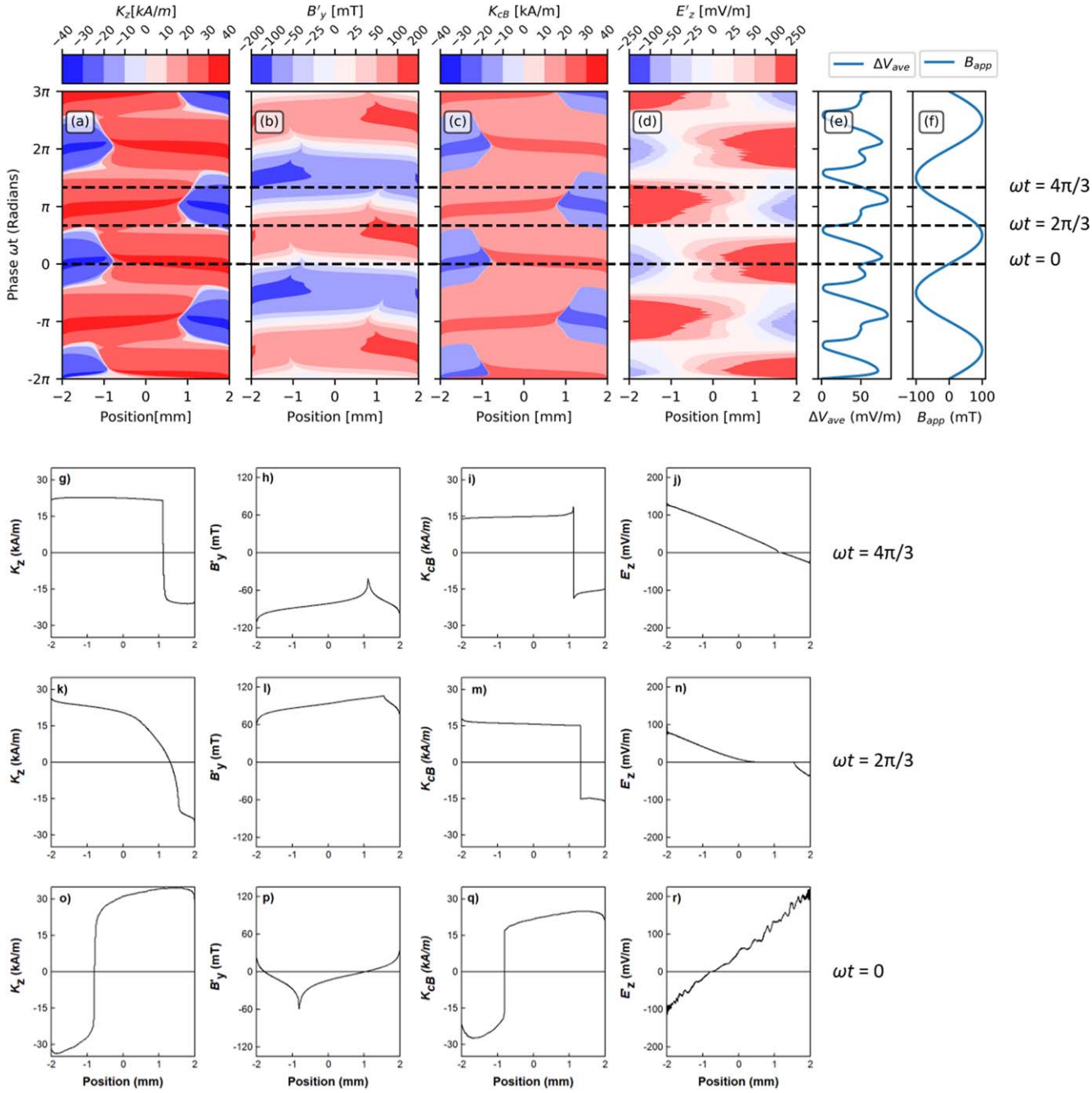

Figure 8. Time evolution of the *interpolated* $J_c(B, \theta)$ model for the SuperPower tape. The sheet variables K_z, B'_y, K_{cB} and E'_z (a)–(d) alongside ΔV (e) and $B_{app}(t)$ (f) are given for two and a half cycles of the applied field. Here $i = 0.5$, $f = 118.66$ Hz and $B_{a0} = 100$ mT. Also shown are the instantaneous profiles across the conductor width for K_z (plots (g)–(o)); B'_y (plots (h)–(p)); K_{cB} (plots (i)–(q)); and E'_z (plots (j)–(r)), at the three moments-in-time indicated by the dashed lines $\omega t = 0$, $2\pi/3$ and $4\pi/3$.

though the SuNAM tape exhibits a substantially stronger $J_c(B, \theta)$ dependence than the SuperPower tape. This emphasises the complex nature of these effects, which are only captured by the detailed finite element model.

6. Scaled constant J_{c0} and interpolated $J_c(B, \theta)$ plots

A final comparison between *constant* J_c and *interpolated* $J_c(B, \theta)$ models is shown in figure 10. Here we compare the voltage waveform, $\Delta V(t)$, obtained from the *interpolated* $J_c(B, \theta)$ model with the waveforms calculated from two different *constant* J_c ($n = 20$) models. The first model used is the $J_c = J_{c0}$ model already presented, whilst the second model sets J_c equal to the minimum value during the cycle, such that $J_c = J_c(B_{a0})$. Figure 10 shows these three models for both SuperPower and SuNAM tapes for the same ratio of $B_{app}/B_{th} \approx 6$, such that $B_{a0} = 60$ mT and 150 mT for the SuperPower and SuNAM cases, respectively (it should be noted that the 150 mT field simulated here for the SuNAM

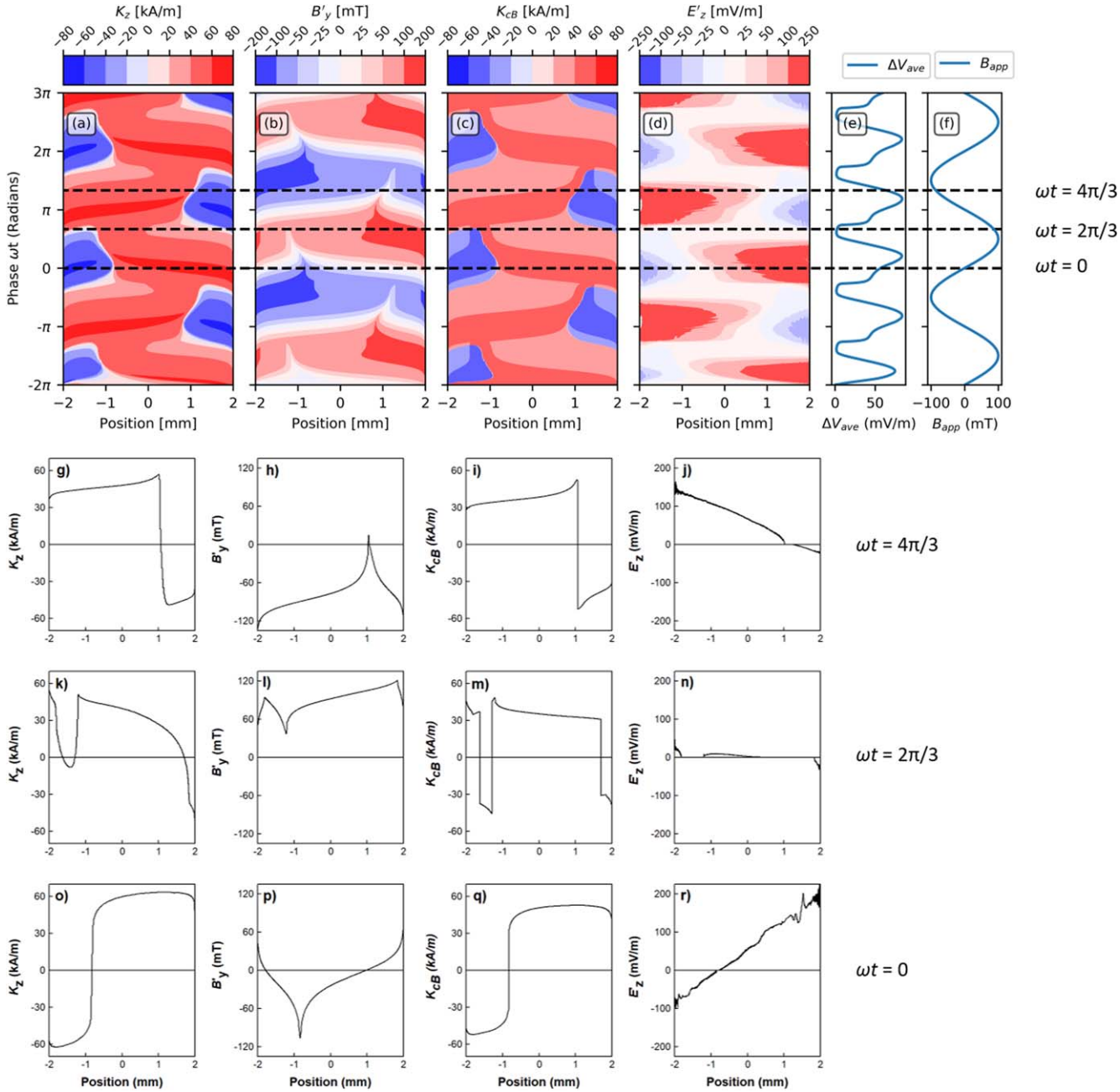

Figure 9. Time evolution of the interpolated $J_c(B, \theta)$ model for the SuNAM tape. The sheet variables K_z , B'_y, K_{cB} and E'_z (a)–(d) alongside ΔV (e) and $B_{app}(t)$ (f) are given for two and a half cycles of the applied field. Here $i = 0.5$, $f = 118.66$ Hz and $B_{a0} = 100$ mT. Also shown are the instantaneous profiles across the conductor width for K_z (plots (g)–(o)), B'_y (plots (h)–(p)), K_{cB} (plots (i)–(q)), and E'_z (plots (j)–(r)) at the three moments-in-time indicated by the dashed lines $\omega t = 0$, $2\pi/3$ and $4\pi/3$.

tape lies beyond the experimentally accessed conditions shown in figure 5).

In both cases, we see that the *interpolated* $J_c(B, \theta)$ waveform is essentially bounded by waveforms obtained from the two *constant* J_c models. The *interpolated* $J_c(B, \theta)$ model predicts the emergence of a non-zero voltage response at the same time as the *constant* $J_c = J_c(B_{a0})$ model and has similar peak values. However, in the sections shaded grey, the *interpolated* $J_c(B, \theta)$ model deviates away from this waveform and instead converges to the *constant* $J_c = J_{c0}$ model. The shaded grey regions denote those times in the cycle during which $B_{app}(t) = 0 \pm B_{th}$, such that the internal magnetic field is small. As such, the approximation $J_c = J_{c0}$ represents a better description of the situation within the tape at these times.

Taken in conjunction with the previous analysis from figures 8 and 9, we therefore conclude that the experimentally-observed peak splitting in $\Delta V(t)$ is due to the periodic increase of $J_c(B, \theta)$ across the entire conductor width at those times in the cycle when $B_{app}(t)$ approaches zero.

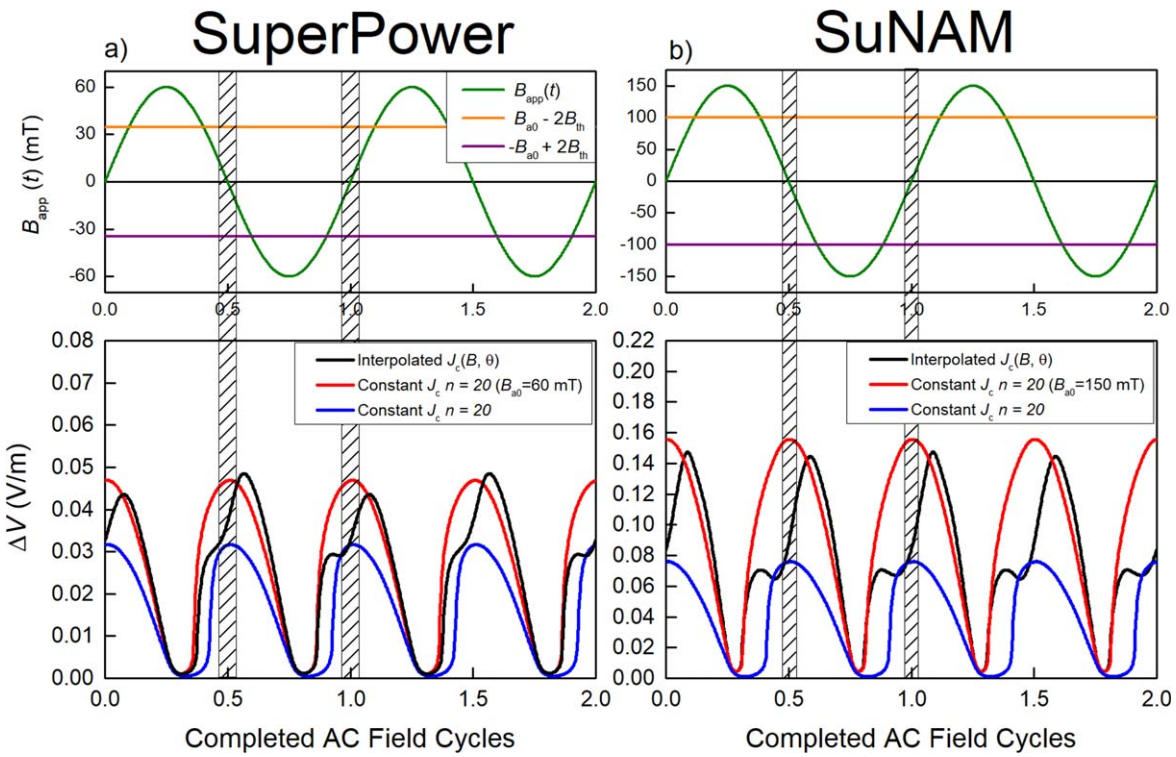

Figure 10. Comparison of the voltage waveform ΔV for (a) SuPower and (b) SuNAM tapes from three different models. Two *constant* J_c models are considered, both of which employ $n = 20$; *Constant* $J_c = J_{c0}$ in blue and $J_c(B_{a0})$ in red. The *interpolated* $J_c(B, \theta)$ model is shown in black. $B_{a0} = 60$ mT in the SuPower case and 150 mT for the SuNAM data. In both cases, $i = 0.5$.

7. Conclusions

In this paper, a 2D numerical FE model based on the *H*-formulation has been used to calculate the transient and DC dynamic resistance generated in two different coated conductor tapes. These modelling results have been analysed and compared with experiment.

In terms of the DC values for the dynamic resistance, the FE model employing a *constant* J_c with a realistic value of $n = 20$ significantly underestimate the experimentally measured values for both the SuPower and SuNAM tapes. By contrast, the FE models which include the full $J_c(B, \theta)$ and $n(B, \theta)$ dependence of the tapes show excellent agreement.

The limitations of the *constant* J_c FE model are further highlighted when the transient time dependent voltage waveforms are compared with experiment. Contour plot visualisations of the time-evolution of the sheet currents and fields within the conductor show a rich variety of features which vary subtly depending on the applied fields and currents, and the specific $J_c(B, \theta)$ dependence. Only the *interpolated* $J_c(B, \theta)$ model is able to reproduce the peak-splitting effect observed in the experimental transient voltage waveforms. This effect arises due to a short-lived increase in the local critical current at the centre of the tape, caused by the varying local magnetic field. As the applied field passes through zero, the critical current at the centre of the tape reaches a maximum thus reducing the local *E*-fields throughout the tape.

It is interesting to note that an FE model approximating to the critical state (where *n* is taken to have a highly elevated value of 200) also shows good agreement with reality. This is despite the fact that neither the *n*-value nor J_c used in this FE model actually correspond to physical reality. Similarly, analytical equations (1)–(3) (which are derived from critical state assumptions [3, 9, 22]) also show excellent agreement with our DC experimental data. A key assumption in the derivation of the analytical equations is that electrical work is performed upon a DC transport current which flows solely in the central region of the tape. However, our FE models show that resistive electric fields extend to the edge of the tape, implying that electrical work is being done throughout the region carrying positive current (i.e. in the same direction as the DC transport current). A corollary of this observation is that it is not possible to spatially distinguish between regions carrying the DC transport current and the screening current flowing in the same direction.

In light of these observations, it is perhaps surprising that the analytical equations based on the critical state do produce such close agreement with the experimental DC values. However, this can be understood by observing that equation (1) simply describes the electrical work required in each cycle to move a net packet of flux across a total DC transport current. The precise location at which this work is done is not relevant to the total work. A similar argument holds for the *constant* J_c ($n = 200$) FE model, which closely approximates to the critical state.

However, the different results obtained using the *constant* J_c ($n = 20$) model are perhaps more puzzling. Following the logic above, this implies that the *constant* J_c FE model predicts that less flux traverses the tape per cycle as the *n*-

value decreases. This suggests that, for the range of experimental conditions examined here, the use of an artificially inflated n-value (e.g. $n = 200$) approximately compensates for the errors incurred by assuming a constant $J_c = J_{c0}$. However, it is not clear that this compensating effect will hold across a broader range of experimental parameters, and indeed there have been a small number of reported experimental results which are not well described by the analytical equations, such as those in [12, 16, 33]. As such, it is expected that the *interpolated* $J_c(B, \theta)$ FE model presented here should generally deliver more reliable results for a coated conductor in an arbitrary field, current and geometry.

Acknowledgments

The Authors would like to acknowledge financial support from New Zealand MBIE Endeavour grant no. RTVU1707, and NZ Royal Society Marsden Grant no. MFP-VUW1806.

MD Ainslie would also like to acknowledge the financial support from an EPSRC Early Career Fellowship EP/P020313/1. All data are provided in full in the results section of this paper.

JM Brooks would like to acknowledge financial support from the Victoria Doctoral Scholarship Scheme, and the Te Āti Hau Trust.

ORCID iDs

J M Brooks https://orcid.org/0000-0001-8586-776X
M D Ainslie https://orcid.org/0000-0003-0466-3680
Zhenan Jiang https://orcid.org/0000-0002-3482-3510
R A Badcock https://orcid.org/0000-0003-0219-9570
C W Bumby https://orcid.org/0000-0001-8555-2469

References

[1] Andrianov V, Zenkevich V, Kurguzov V, Sytchev V and Ternovskii F 1970 Effective resistance of an imperfect type-II superconductor in an oscillating magnetic field *Sov. Phys.—JETP* **31** 815

[2] Aikele M, Huebener R, Weischer D and Tsuei C 1997 Effect of high-frequency magnetic fields on the dissipative vortex motion in the superconducting mixed state *Physica* C **290** 109–12

[3] Oomen M, Rieger J, Leghissa M, ten Haken B and ten Kate H H 1999 Dynamic resistance in a slab-like superconductor with $J_c(B)$ dependence *Supercond. Sci. Technol.* **12** 382

[4] Ogasawara T, Yasukōchi K and Sayama S 1976 Effective resistance of current carrying superconducting wire in oscillating magnetic fields: II. Twisted multifilamentary composite conductor *Cryogenics* **16** 89–96

[5] Geng J and Coombs T 2015 Mechanism of a high-T_c superconducting flux pump: using alternating magnetic field to trigger flux flow *Appl. Phys. Lett.* **107** 142601

[6] Geng J, Matsuda K, Fu L, Fagnard J-F, Zhang H, Zhang X, Shen B, Dong Q, Baghdadi M and Coombs T 2016 Origin of DC voltage in type-II superconducting flux pumps: field, field rate of change, and current density dependence of resistivity *J. Phys. D: Appl. Phys.* **49** 11LT01

[7] Jiang Z, Hamilton K, Amemiya N, Badcock R and Bumby C 2014 Dynamic resistance of a high-T_c superconducting flux pump *Appl. Phys. Lett.* **105** 112601

[8] Jiang Z, Bumby C W, Badcock R A, Sung H-J, Long N J and Amemiya N 2015 Impact of flux gap upon dynamic resistance of a rotating HTS flux pump *Supercond. Sci. Technol.* **28** 115008

[9] Bumby C, Jiang Z, Storey J, Pantoja A and Badcock R 2016 Anomalous open-circuit voltage from a high-T_c superconducting dynamo *Appl. Phys. Lett.* **108** 122601

[10] Ciszek M, Knoopers H, Rabbers J, Ten Haken B and Ten Kate H H 2002 Angular dependence of the dynamic resistance and its relation to the AC transport current loss in Bi-2223/Ag tape superconductors *Supercond. Sci. Technol.* **15** 1275

[11] Ciszek M, Tsukamoto O, Ogawa J and Miyagi D 2002 Energy losses in YBCO-123 coated conductors carrying transport current in perpendicular external magnetic field *AIP Conf. Proc.* **614** 606–13

[12] Duckworth R C, Zhang Y F, Ha T and Gouge M J 2010 Dynamic resistance of YBCO-coated conductors in applied ac fields with DC transport currents and DC background fields *IEEE Trans. Appl. Supercond.* **21** 3251–6

[13] Jiang Z, Toyomoto R, Amemiya N, Bumby C W, Badcock R A and Long N J 2016 Dynamic resistance measurements in a GdBCO-coated conductor *IEEE Trans. Appl. Supercond.* **27** 1–5

[14] Jiang Z, Toyomoto R, Amemiya N, Zhang X and Bumby C W 2017 Dynamic resistance of a high-T_c coated conductor wire in a perpendicular magnetic field at 77 K *Supercond. Sci. Technol.* **30** 03LT01

[15] Jiang Z, Zhou W, Li Q, Yao M, Fang J, Amemiya N and Bumby C W 2018 The dynamic resistance of YBCO coated conductor wire: effect of DC current magnitude and applied field orientation *Supercond. Sci. Technol.* **31** 035002

[16] Uksusman A, Wolfus Y, Friedman A, Shaulov A and Yeshurun Y 2009 Voltage response of current carrying YBCO tapes to alternating magnetic fields *J. Appl. Phys.* **105** 093921

[17] Geng J, Yang J, Gawith J, Shen B, Ma J and Coombs T 2019 Second harmonic in the voltage of DC-carrying YBCO tape under a perpendicular alternating magnetic field *Physica* C **564** 11–6

[18] Norris W 1970 Calculation of hysteresis losses in hard superconductors carrying AC: isolated conductors and edges of thin sheets *J. Phys. D: Appl. Phys.* **3** 489

[19] Brandt E, Indenbom M and Forkl A 1993 Type-II superconducting strip in perpendicular magnetic field *EPL* **22** 735

[20] Brandt E H and Indenbom M 1993 Type-II superconductor strip with current in a perpendicular magnetic field *Phys. Rev.* B **48** 12893

[21] Zeldov E, Clem J R, McElfresh M and Darwin M 1994 Magnetization and transport currents in thin superconducting films *Phys. Rev.* B **49** 9802

[22] Mikitik G P and Brandt E H 2001 Generation of a DC voltage by an AC magnetic field in type-II superconductors *Phys. Rev.* B **64** 092502

[23] Plummer C and Evetts J 1987 Dependence of the shape of the resistive transition on composite inhomogeneity in multifilamentary wires *IEEE Trans. Magn.* **23** 1179–82

[24] Rhyner J 1993 Magnetic properties and AC-losses of superconductors with power law current-voltage characteristics *Physica* C **212** 292–300

[25] Clem J R 1970 Theory of flux-flow noise voltage in superconductors *Phys. Rev.* B **1** 2140

[26] Jackson J D 1999 *Classical Electrodynamics* 3rd edn (New York: Wiley)

[27] Ainslie M D, Bumby C W, Jiang Z, Toyomoto R and Amemiya N 2018 Numerical modelling of dynamic resistance in high-temperature superconducting coated-conductor wires *Supercond. Sci. Technol.* **31** 074003

[28] Wimbush S C and Strickland N M 2016 A public database of high- temperature superconductor critical current data *IEEE Trans. Appl. Supercond.* **27** 1–5

[29] Strickland N, Hoffmann C and Wimbush S 2014 A 1 kA-class cryogen-free critical current characterization system for superconducting coated conductors *Rev. Sci. Instrum.* **85** 113907

[30] Zermeño V M, Habelok K, Stepien M and Grilli F 2017 A parameter-free method to extract the *superconductor's* $J_c(B, \theta)$ field-dependence from in-field current–voltage characteristics of high temperature superconductor tapes *Supercond. Sci. Technol.* **30** 034001

[31] Hu D, Ainslie M D, Rush J, Durrell J H, Zou J, Raine M and Hampshire D 2015 DC characterization and 3D modelling of a triangular, epoxy-impregnated high temperature superconducting coil *Supercond. Sci. Technol.* **28** 065011

[32] Hu D, Ainslie M D, Raine M J, Hampshire D P and Zou J 2016 Modelling and comparison of in-field critical current density anisotropy in high-temperature superconducting (HTS) coated conductors *IEEE Trans. Appl. Supercond.* **26** 1–6

[33] Jiang Z, Zhou W, Bumby C, Staines M, Li Q, Badcock R, Long N and Fang J 2017 Dynamic resistance measurement of a four-tape YBCO stack in a perpendicular magnetic field *IEEE Trans. Appl. Supercond.* **28** 1–5

[34] Matsushita T 1994 *Flux Pinning and Electromagnetic Phenomenon* (Tokyo: Sangyo Tosho Inc.) p 99

[35] Shen Boyang, Li Jing, Geng Jianzhao, Fu Lin, Zhang Xiuchang, Li Chao, Zhang Heng, Dong Qihuan, Ma Jun and Coombs T.A. 2017 Investigation and comparison of AC losses on stabilizer-free and copper stabilizer HTS tapes *Physica C: Superconductivity and its Applications* **541** 40–44

[36] Liu Guole, Zhang Guomin, Yu Hui, Jing Liwei, Ai Liwang and Liu Qi 2017 Experimental and numerical study of frequency-dependent transport loss in YBa2Cu3O7–δ coated conductors with ferromagnetic substrate and copper stabilizer *Journal of Applied Physics* **121** 243902

[37] Sundaram A *et al* 2016 2G HTS wires made on 30μm thick Hastelloy substrate *Superconductor Science and Technology* **29** 104007

[38] Lee Jae-Hun, Lee Hunju, Lee Jung-Woo, Choi Soon-Mi, Yoo Sang-Im and Moon Seung-Hyun 2014 RCE-DR, a novel process for coated conductor fabrication with high performance *Superconductor Science and Technology* **27** 044018